A combined strategy for landmine detection and identification using synthetic GPR responses

Maria A. Gonzalez-Huici *, Fabio Giovanneschi

Fraunhofer Institute for High Frequency Physics and Radar Techniques, 53343 Wachtberg, Germany

A B S T R A C T

Synthetic Ground Penetrating Radar (GPR) target responses may be successfully used for buried landmine classification purposes. This paper demonstrates that accurately simulated one-dimensional temporal signatures can be employed as reference waveforms for efficient clutter suppression and improved target detection/recognition. The proposed methodology is a combined approach consisting of a cross-correlation based identification algorithm and an energy based detection algorithm. The former can be implemented before conducting the detection as an additional filtering step in the form of a similarity constraint between measured and synthetic scattered signals. The application of the combined method to experimental data yields a clear gain in the detection sensitivity, particularly for those mines which are most difficult to detect through scattered energy considerations alone. Moreover, an adapted Inverse Distance Weighted (IDW) averaging has been incorporated to enhance the quality of the imaging and to rise the Signal-to-Clutter ratio (SCR) of the resulting maps. This strategy can help to substantially reduce the number of false alarms and speed up the clearance labors.

© 2013 Elsevier B.V. All rights reserved.

1. Introduction

Antipersonnel mines (APM) represent one of the worst kinds of global pollution. The use of conventional metal-detectors in demining operations may become particularly slow and inefficient because of the low-metal content of several modern landmines and the presence of abundant metallic scrap in battlefields. Therefore, alternative methods have been intensively investigated in the past years. The Ground Penetrating Radar (GPR), which is a very popular tool for underground noninvasive imaging, has demonstrated good potential for the detection of all types of landmines due to its sensitivity to any contrast in the electromagnetic properties of the soil (Daniels, 2007). Nevertheless, the detection of plastic landmines with GPR remains a challenging task: the weak responses produced by the low-contrast small mines are frequently obscured by other undesirable effects (clutter) from antenna coupling, system ringing and rough surface/inhomogeneous soil reflections.

There are different processing techniques to overcome the problem of landmine detection and identification in realistic scenarios. For target detection a model of the background can be defined and all the reflections that clearly differ from the estimated background signal are declared as targets (Gader et al., 2004). Some methods that have shown good potential to take the target/background decision and reduce the clutter are for example a statistical binary hypothesis testing

(Uschkerat, 2000), wavelet transform (Carevic, 2000) or independent component analysis (Karlsen et al., 2002). Another strategy, which is the one followed in this paper, is to establish a clutter level according to the average amount of scattered energy at each depth, and the detection is called when a cluster or a single pixel supersedes sufficiently this level. However, it must be noted that all these approaches are not capable of discriminating between a landmine and other reflectors present in soil (such as munition fragments, roots, stones), hence the false alarm rate increases and additional processing becomes necessary to identify anomalies. Regarding target classification, the common approach relies on defining a target model given by a target feature vector which is searched in the GPR data (Potin et al., 2006; Shao et al., 2013). These vectors may be based on single one-dimensional (1D) target echoes or on characteristic 2D or 3D target traces spread along the scans. The search of scattering features in the data can be implemented in different ways, including Fuzzy Logic approaches (Wilson et al., 2007), Neural Networks (Yang and Bose, 2005), Markov Models (Gader et al., 2001) or Support Vector Machines (Massa et al., 2005; Shao and Bouzerdoum, 2011).

This work presents a signal processing procedure which involves target models based on the shape of the scattered 1D signals (A-scans) in a first recognition phase, and an energy-based detection algorithm which takes into account the amplitude information in a second phase. The outputs from both algorithms have been improved by IDW averaging where the attribute value of each individual pixel is substituted by a properly weighted average value of the information contained in it and within its surrounding area.

* Corresponding author.
  E-mail address: maria.gonzalez@fhr.fraunhofer.de (M.A. Gonzalez-Huici).

The organization of the paper is as follows. Section 2 is a brief introduction to some GPR modeling issues concerning the software and the GPR model utilized to synthesize the radar responses. Section 3 contains the measurement details regarding the test site characteristics, the buried targets and the acquisition parameters. Section 4 describes the recognition and detection algorithms as well as the combined processing strategy together with the achieved results. Finally, the conclusions are presented in Section 5.

2. GPR modeling

Since analytical solutions of the GPR problem are restricted, numerical forward modeling is crucial to compute synthetic responses. A reliable estimation of the radar echoes and performance in general (especially in near field conditions), requires to model simultaneously all the elements in the GPR scene, i.e. antennas, soil and targets, in an accurate way. Only then, a direct comparison between simulated and measured signals is possible.

The synthetic signatures for this work were obtained using COMSOL, a finite element method based commercial tool for multiphysics modeling which is suitable for solving complex GPR scenarios. The equipment employed for the experimental investigation is an impulse GPR system built by ERA Technology and 2 GHz emission bandwidth.

In particular, the antenna unit consists of two identical bowtie–dipole antennas placed side-by-side and enclosed in a shielding case filled with absorbing material. In order to introduce the real illumination in the COMSOL simulations, the radar antenna model was optimized and validated by means of laboratory measurements (in free space) until a satisfactory agreement between measured and synthetic responses was reached (Gonzalez-Huici and Uschkerat, 2010). Together with a precise antenna model, exact CAD representations of the targets and realistic soil characteristics were included in the GPR model.

3. Measurements

3.1. Test site description

To assess the performance of the proposed approach in realistic conditions, a measurement campaign was carried out in a prepared test field of the Leibniz Institute for Applied Geophysics (LIAG) in Hannover (Germany). A picture of the field is shown in Fig. 1 where arrows point to the lane where the targets were buried. In the left side of the figure, there is a detailed layout of the test area. Here the red squares correspond to 1×1 m survey areas scanned in every measurement. The targets in the left line (red points with odd numbers) are buried approx. 5 cm depth and the targets in the right line (red points with even numbers) lie approx. 10 cm depth. The bold lines with numbers starting in 200 and 300 respectively, designate the plastic rails at the borders of the test lane and the reference positions for the measurements in centimeters. The zero point of the coordinates is located on the right corner of the left rail and it is indicated with a red circle.

The grassy surface presented moderate roughness and the soil texture was sandy and highly inhomogeneous due to the presence of organic material, stones, etc. Hence, the resulting non constant moisture content and irregular upper subsurface, led to a notorious variability of the electrical parameters (in particular the permittivity), elevating significantly the clutter contributions in our radar data.

The dielectric constant was measured at three different days in August and September with a Time Domain Reflectometer (TDR) along a 12 m long line every 10 cm. The average value oscillated between 4.6 in August and 10.1 in September with ~15% standard deviation and correlation length of ~20 cm. The days of the campaign the average permittivity was around 7.

3.2. Acquisition parameters

The main acquisition parameters during the LIAG campaign are summarized in Table 1.

3.3. Test targets

In the referred test field, there were four different buried targets: three landmine simulants (PMN, PMA-2 and Type-72) and a Standard Test Target (ERA test target). In this study the focus is especially on three of them: the PMN simulant, the Type-72 simulant and the ERA test target, whose pictures and the corresponding CAD models used for the simulations are illustrated in Fig. 2.

4. Methodology and results

The proposed approach is a processing methodology consisting of a target recognition technique and an energy based detection technique which can be applied separately or in combination (see Fig. 3). More specifically, the recognition algorithm incorporates a similitude constraint that sets equal to zero those traces which locally deviate from the target model in a relevant manner; in this way, the significant data volume is reduced and several undesired echoes (clutter) are suppressed. On the other hand, the detection algorithm determines the average energy value for every depth slice (C-scan) and then, those pixels whose amplitudes are not sufficiently above this value are set to zero. Thus, the contributions which may be associated to noise even if they present a high correlation degree with a reference target, are eliminated. The last step is to perform the sum of all the resulting C-scans over a certain time interval in order to get the final detection maps.

Additionally, a weighted averaging is applied to the data in order to improve the performance of the strategy.

4.1. Recognition

In order to simplify and accelerate the target recognition procedure, the proposed algorithm uses single one-dimensional (1D) scattered signals. These waveforms are employed in the similarity assessment.

4.1.1. Cross-correlation

A measure of the similarity between a given signal $u(t)$ and a reference $v(t)$ is well-known by means of their cross-correlation function,

$$R_{uv}(\tau) = \int u(t-\tau)v(t)dt = u(-t) * v. \qquad (1)$$

This function determines the analogy between two non-identical waveforms as a function of the time shift τ between them and can reveal similarities undetectable by other techniques. The cross-correlation can be approximated via the sampling method:

$$R_{uv}(\tau) = \frac{1}{N}\sum_{n=1}^{N} u(n\Delta t-\tau)v(n\Delta t). \qquad (2)$$

Table 1
GPR system acquisition parameters.

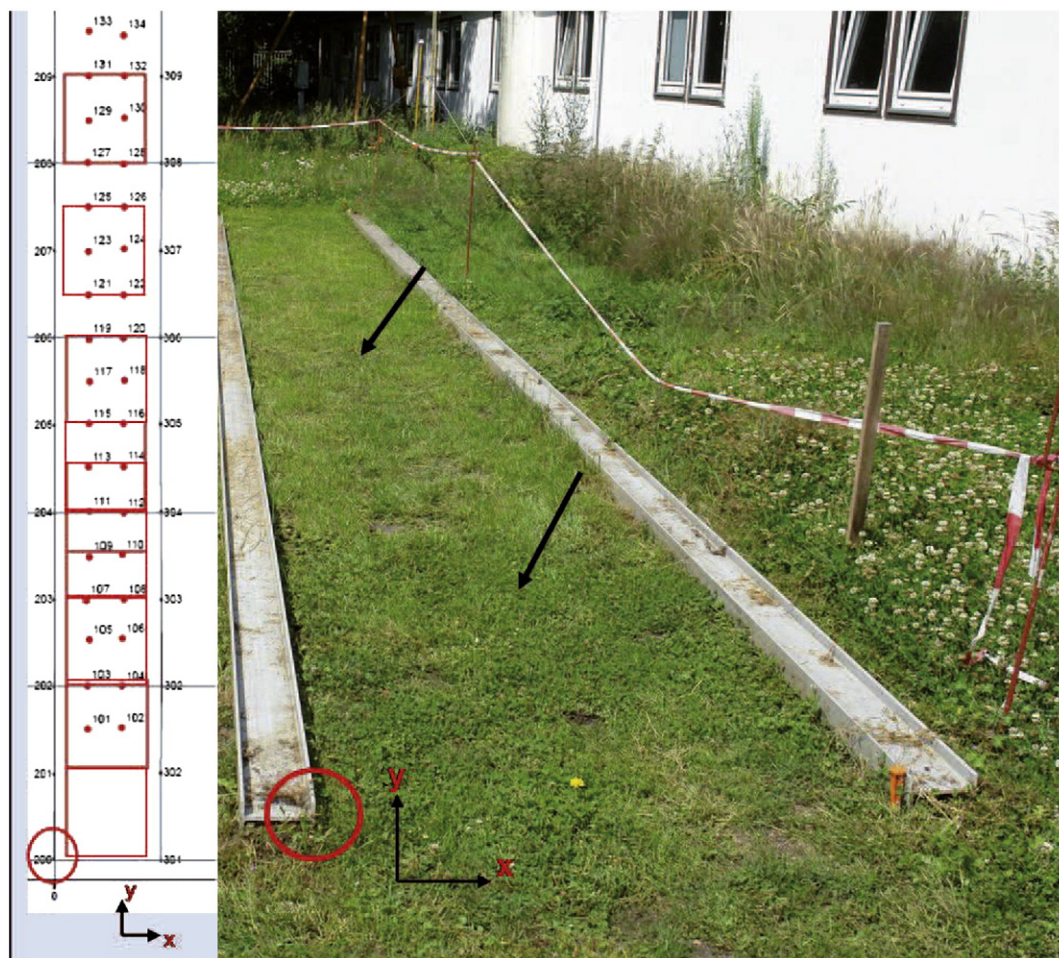| GPR type	Impulse radar
Central frequency	2 GHz
PRF	1 MHz
Pulse length	0.5 ns
Sampling time	25 ps
Spatial sampling in X/Y	1 cm/4 cm
Antenna height	5–9 cm
Antenna configuration	Perpendicular broadside
Samples/scan	512/A-scan

Fig. 1. Test area layout and targets' position (left) and test field with buried test mines indicated by arrows (right).

The previous definition shows that the cross-correlation is essentially an averaged sum of the term by term product of one waveform and the delayed version of the second waveform. It depends linearly on the magnitude of the input signal $u(t)$. However, for our purpose, merely the shape information is relevant since neither the signal amplitude nor its energy represents a feature for the target model. Then, a
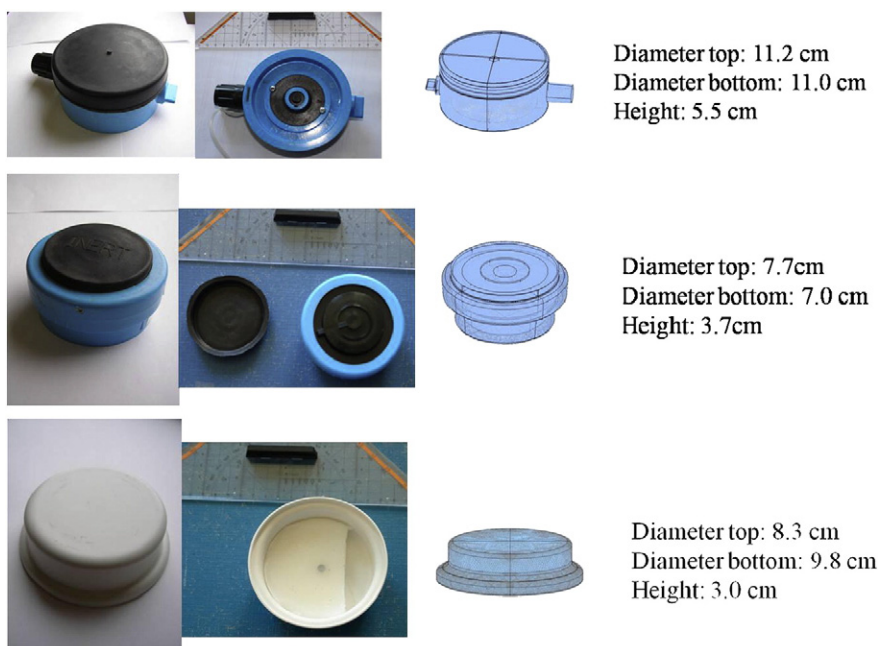

Fig. 2. PMN simulant (top), Type-72 simulant (middle) and ERA test target (bottom) utilized in the measurements and their CAD models.
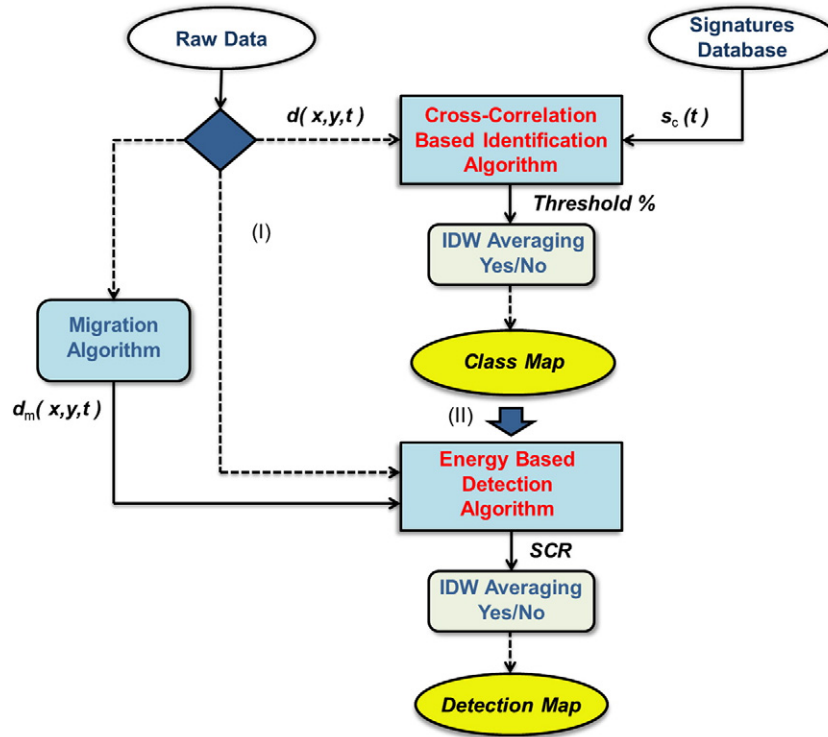
Fig. 3. Block diagram of the proposed methodology.

normalization of the input and reference waveforms is required before the comparison of the waveforms. Nevertheless, to carry out the input signal normalization is not a trivial issue because the target response usually does not possess the highest amplitude in the trace, particularly if the direct coupling and the surface reflection are not removed. Thus, in order to keep only the shape information, the input signal should be windowed in time and normalized before carrying out the similarity measure:

$$\bar{u}(t,T) = \begin{cases} \dfrac{u(T)}{max\{|u(T)|\}}, & \text{for} \quad t_1 \leq T \leq t_2 \\ 0, & \text{otherwise} \end{cases} \quad (3)$$

where $\bar{u}(t,T)$ is the new input signal for the cross-correlation calculation and T is the time window.

Applying this method, the discrete cross-correlation of a normalized portion of a measured A-scan and a high-quality normalized reference echo (which is obtained by accurate numerical modeling) is determined. Then, the maximum absolute value of the cross-correlation vector determines the correlation coefficient ρ_{uv} between both waveforms:

$$\rho_{uv} = max\{|R_{uv}|\} \quad (4)$$

4.1.1.1. Measurements vs. simulations. To evaluate the achieved correspondence degree between accurate reference signatures and actual signatures, some tests were carried out in laboratory using the test mines illustrated in Fig. 2. The cross-correlation is computed for a sequence $2N-1$ time shifts $T(m-N)$ where $m = 1,...,2N-1$ and N is the length of the vectors u and v.

Fig. 4 displays the comparison between both, synthetic and measured normalized signals of the considered test mines and the corresponding cross-correlation measure between both waveforms in free space. The scattering signatures are obtained subtracting the simulated/measured

signal without target from the scattered simulated/measured signal with target for each of the cases. The material electrical parameters to simulate the test mines are taken from (von Hippel, 2005).

The different plots show a high correlation coefficient between simulations and measurements for all the three objects analyzed. Even for the PMN, which is the one with most complex internal structure, a correlation coefficient of 95% was attained.

4.1.2. Class map

The class map is a classified image comprised of a mosaic of pixels, which are color-coded according to the target class they belong to. To elaborate this kind of map the cross-correlation is performed trace by trace with all the reference waveforms present in the database. The values of the correlation coefficient obtained for each reference signature in the survey area define a data level (slice) C^k for that area. Besides, the pixels where these coefficients are below a certain similitude threshold are set to zero, so that the data level for a reference target k (class) is given by:

$$C^k(x,y) = \begin{cases} \rho^k(x,y) & \text{if} \quad \rho^k(x,y) > \text{Threshold} \\ 0, & \text{otherwise} \end{cases} \quad (5)$$

where k is the corresponding reference class for that data level. Each individual pixel of the final map is then classified based on this similarity information. For those samples with a zero in all the data levels, the corresponding cell is declared as empty, i.e., the assigned *Class* is "No object". For the rest of pixels, the class declaration *Class* corresponds to the most similar reference target, which is the object from the database whose synthetic signature has the highest correlation coefficient with the considered trace:

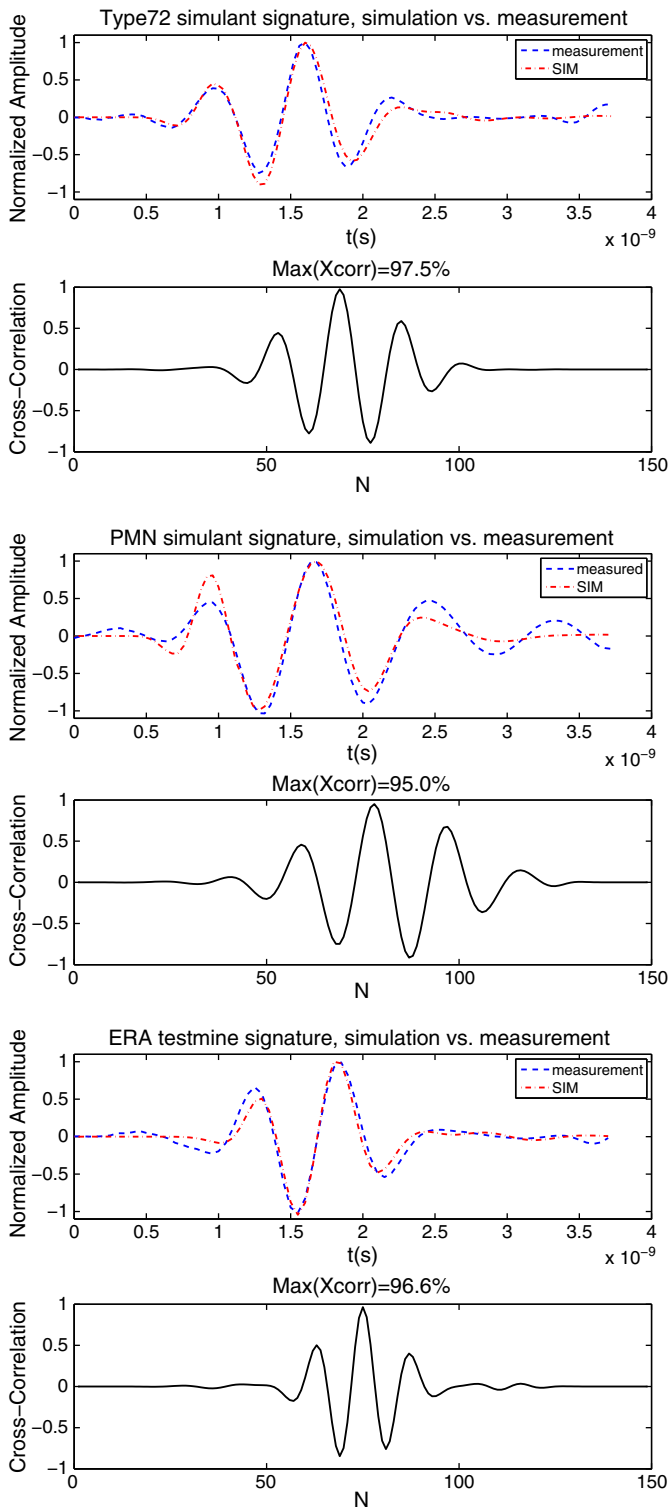$$\textit{Class}\,(x,y) = \max_{k}\,\left\{C^k(\pi x,y)\right\}. \quad (6)$$

Fig. 4. Cross-correlation between measured and simulated signatures for a Type-72 simulant (top), a PMN simulant (middle) and an ERA test target (bottom).

As an example, Fig. 5 illustrates two of the computed class maps for one survey with buried PMA-2 simulants (not present in our synthetic database) and another one with buried ERA test targets.

In the middle of both images there are aggregates of colored pixels, which correspond with the position of the real targets. These class maps evidence the presence of buried objects and may be able to identify them correctly. In the directory of the database considered for the

correlation calculation, there were 20 simulated waveforms for the three landmine simulants and a few canonical clutter objects buried in dry and wet soil at two different depths. For instance, none of the metallic objects in the database are declared in the maps, since their waveforms are not similar enough to any of the traces in the surveys. In the case of SVY-139 (top), there is no reference waveform in the database for the mine PMA-2 and the mine is incorrectly declared but detected. This happens because the similar dimensions of the mines and all the clutter objects considered give rise to rather coincident signatures. In particular, the bottom mine is identified as a Type-72 which has almost the same height as the actual PMA-2. In the second example, a survey with a particularly high clutter level (SVY-147) is selected. As it will be shown in the section about detection, in this particular survey it is rather difficult to detect the bottom mine based only on the scattered energy. On the other hand, when the identification procedure is performed, the corresponding class map shows two ERA test targets in the middle of the image, which agrees with the reality. However, in both class maps, several pixels remain incorrectly identified. In particular, there are some clusters of pixels where different classes are found in very small areas. Ideally, there should be just one object class declaration per cluster unless there are two or more objects at different depths in the same or almost the same area segment. In order to improve the class selection performance, an image processing technique is proposed below, which builds the data level for each reference target considering the correlation coefficient values not only for individual cells (locations) in the survey but also for the neighbor cells.

4.1.2.1. Application of Inverse Distance Weighted (IDW) averaging. As mentioned before, our aim is to determine the target class which presents maximum analogy with the considered trace. Since the scattered energy by a given reflector will show up in several traces over a certain halo (corresponding to the region where the scatterer is located and slightly around), it is desirable to take also into account the similarity information of the neighbor pixels. To properly consider all the pixels within the neighborhood of the processing pixel, some weights need to be applied to the different contributions so that the closer a pixel is to the evaluated one, the more influence it has on its estimated final value. To do this, an easy and fast technique widely used by geoscientists is chosen here: the so called Inverse Distance Weighted (IDW) spatial interpolation technique. Formally, the IDW method derives the attribute value $\overline{u}(x, y)$ at the location (x, y), given the observed u values sampled at (x_i, y_j) in the following manner (Lu and Wong, 2008):

$$\overline{u}(x, y) = \sum_{i,j} w_{ij} u_{ij}, \tag{7}$$

where w_i corresponds to the weight factor that controls the relative importance of the point u_{ij} in the interpolation. This weight is usually defined as

$$w_{ij} = \frac{d_{xy,ij}^{-p}}{\sum_{ij} d_{xy,ij}^{-p}}, \tag{8}$$

where $d_{xy,ij}$ is the Euclidean distance between $u(x,y)$, u_{ij}, and $\sum_{ij} w_{ij} = 1$.

Essentially, the general idea is based on the assumption that the value at (x,y) is the weighted average of observed u values within its neighborhood, and the weights are inversely related to the distances between the prediction point and the sampled data points (Lu and Wong, 2008). The inverse distance weight can be modified by an arbitrary constant power p (typically, $p = 2$) to adjust the diminishing strength in relationship with increasing distance, which is often called "Shepard's Method" (Shepard, 1968).

To apply this method to build a class map, first an area surrounding each pixel (halo) is selected, whose dimensions are set according to the size of the present targets. In particular, for cylindrical mines of
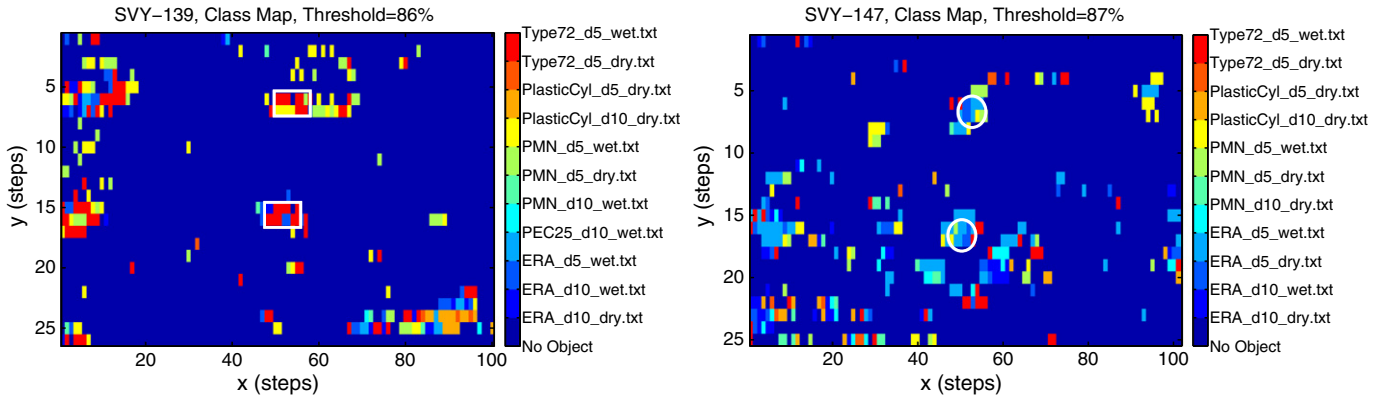
Fig. 5. Class maps of surveys SVY-139 (left) and SVY-147 (right). The targets in the middle of SVY-139 are PMA-2 simulants and the targets in the middle of SVY-147 are ERA test targets.

diameter between 7 and 11 cm, a halo of 11 cm × 12 cm horizontal and vertical length is considered. Then, according to Eq. 7 and Eq. 8, the averaged correlation data level for a particular target class k will take the form below:

$$\overline{C}^k(x,y) = \frac{\sum\limits_{i,j} d_{xy,ij}^{-2} \rho_{ij}^k}{\sum\limits_{i,j} d_{xy,ij}^{-2}}, \qquad (9)$$

where (x,y) refers to the evaluated location, i and j are the coordinates of the considered pixel within the halo, ρ_{ij}^k is its correlation coefficient and $d_{xy,ij}$ is the distance between each sampled pixel and the geometrical center of the halo.

Next, the obtained weighted average at every evaluation point is compared with the selected similitude threshold, canceling all those values below it:

$$\overline{C}^k(x,y) = \begin{cases} \overline{C}^k(x,y) & \text{for } \overline{C}^k(x,y) > \text{Threshold} \\ 0, & \text{otherwise} \end{cases} \qquad (10)$$

Finally, in order to obtain a class map out of the new data matrix $\overline{C}$, the algorithm looks for the maximum among all the class levels at the different survey positions (x,y):

$$Class\,(x,y) = \max_k \left\{ \overline{C}^k(x,y) \right\}. \qquad (11)$$

Fig. 6 displays the correlation maps achieved applying the proposed averaging technique to the same surveys analyzed in the previous section. As it can be observed, there is a clear improvement in the images regarding both, false alarm reduction and target discrimination

capability. In particular, this method reduces the number of different target assignments within small areas along with the number of single pixel target declarations, i.e., clutter contributions.

Therefore, even if more tests with experimental data are still necessary together with a more accurate and large signature database, the authors strongly think that this technique shows a good potential for target recognition applications.

4.2. Detection

Recorded amplitudes and arrival times of the reflected signals are the first information used to interpret GPR data. In particular, the magnitude of the signal mainly depends on the size and depth of the reflector and on its dielectric contrast with the background medium. Hence, the scattered energy amplitude is the easiest and more direct way of detecting the presence of a target.

4.2.1. Energy based detection algorithm

The detection algorithm introduced in this section relies on scattered energy information. Basically, it consists in normalizing the pixel energy with respect to the maximum amplitude per C-scan; set the required SCR energy threshold above the average pixel amplitude per C-scan; set to zero all the pixels below this level (which corresponds to the estimated clutter level at every depth) in order to keep only the most "brilliant" pixels; and finally, integrate over a time (depth) interval all the resulting C-scans, thus obtaining the so called 2D detection map. This algorithm can be formulated as follows:

$$|I(x,y;t)| = \begin{cases} |I(x,y;t)| & \text{if } 10\log\left[\dfrac{|I(t)|}{E_\Omega(|I(t)|)}\right]^2 > \text{SCR} \\ 0, & \text{otherwise} \end{cases} \qquad (12)$$
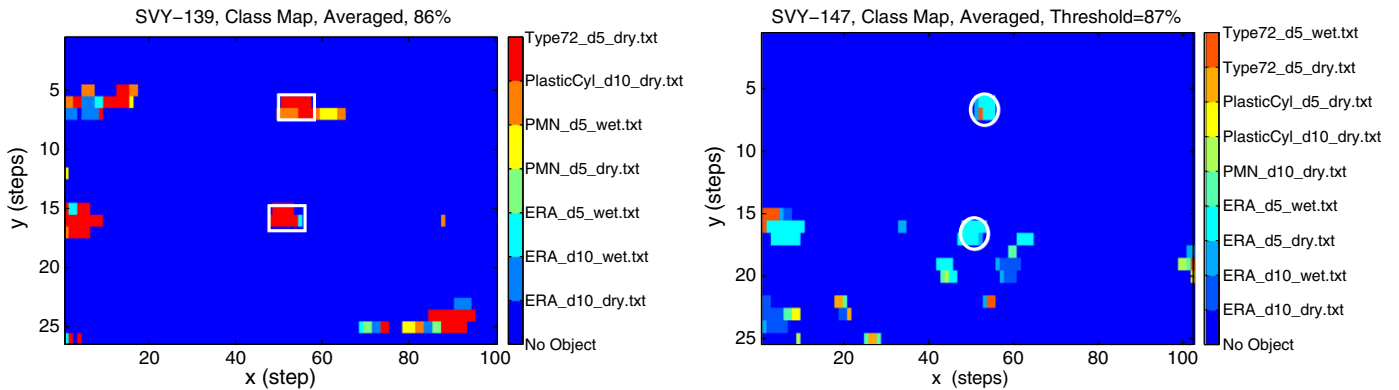

Fig. 6. Class maps of surveys SVY-139 (left) and SVY-147 (right) with IWD averaging. The targets in the middle of SVY-139 are PMA-2 simulants and the targets in the middle of SVY-147 are ERA test targets.
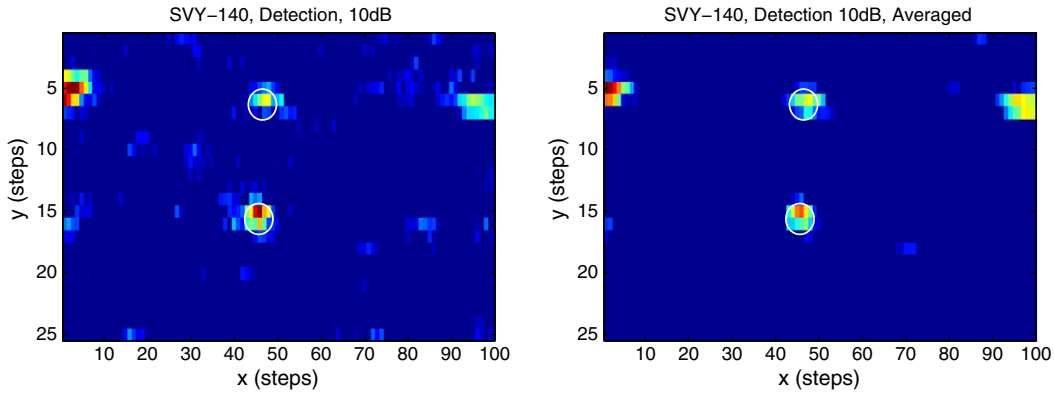
Fig. 7. Detection map without (left) and with IWD averaging (right) over a survey area with buried PMN simulants.

where $|I|$ is the absolute value of the recorded signal (preprocessed or not) per pixel, x, y are the spatial coordinates and t the arrival times, SCR corresponds to the Signal-to-Clutter ratio in dB, $E(\cdot)$ is the expectation operator and $\Omega \subset (x,y)$ is the slice area.

Next, the aforementioned detection map can be calculated by the following sum over depth:

$$D(x,y;T) = \sum_{t=t_1}^{t_2} |I(x,y;t)|, \qquad (13)$$

with $T = t_2 - t_1$ being the width of the time window considered for the detection.

It is possible to obtain 3D images of the detected targets performing the sum given by Eq. 13 for successive and very short time intervals, i.e., considering a sliding window (with preferably a certain overlap) along the whole desired investigation depth. This operation results in a collection of detection maps for successive depth intervals that can be displayed in 3D. Such volume representation would allow the viewer to localize the objects inside the whole imaging domain, giving him an impression of the target's real depth and dimension.

Before the application of the detection algorithm to the field surveys, the only preprocessing performed is a digital bandpass frequency filter and a DC removal. An average background subtraction is not always necessary neither recommended, due to the high degree of inhomogeneity of the upper subsurface. Instead, the traces are windowed in time in order to partially remove the surface reflection and antenna crosstalk. In most cases with the biggest targets present (PMN and PMA-2), the backscattered signal is enough strong to result in clear detections even when summing over the entire time axis without any windowing.

To quantify the detectability of the different test mines in the LIAG test field, we will also generate the Receiver Operating Characteristic (ROC) curves associated to the surveys with buried mines of the same class separately. The probability of detection (Pd) and the false alarm rate (FAR) are derived according to the following expressions:

$$Pd = \frac{\text{Number of detected mines}}{\text{Total number of mines}}, \qquad (14)$$

$$FAR = \frac{\text{Number of detected pixels outside the target halo}}{\text{Total number of pixels outside the target halo}}. \qquad (15)$$

The target halo assumed for a true detection is 12 cm × 12 cm in all cases. A mine is declared as detected if there is more than one detected pixel inside the target halo while a false alarm corresponds to a detected pixel with location outside any target halo.

4.2.1.1. Application of IDW averaging. The performance of the energy-based detection algorithm can be improved using the IDW averaging technique already introduced in the prior section. In particular, the idea is to consider the energy information within the neighborhood of each individual pixel for every depth slice before performing the energy thresholding given in Eq. 12. To do it, Eq. 7 and Eq. 8 can be applied to obtain a weighted averaged energy value per pixel as follows:

$$|\bar{I}(x,y;t)| = \frac{\sum_{i,j} d_{xy,ij}^{-2} |I_{ij}(t)|}{\sum_{i,j} d_{xy,ij}^{-2}} \qquad (16)$$

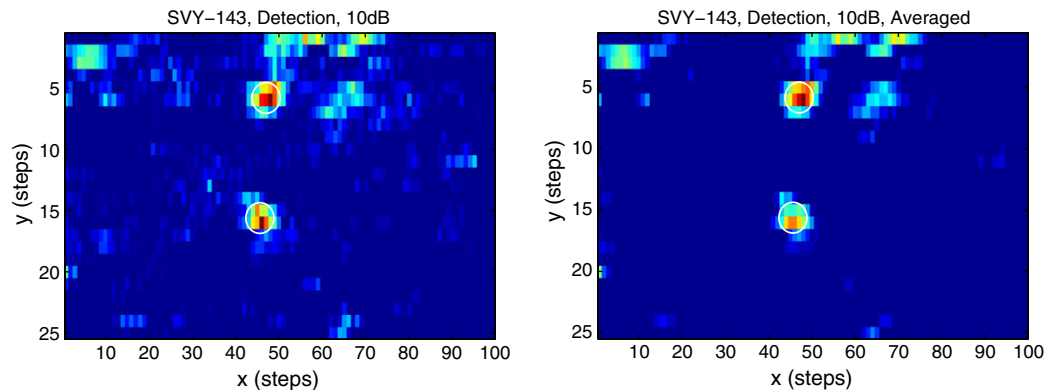where $|\bar{I}|$ is now the new averaged energy input to compute the detection map.

Fig. 8. Detection map without (left) and with IWD averaging (right) over a survey area with buried ERA test targets.
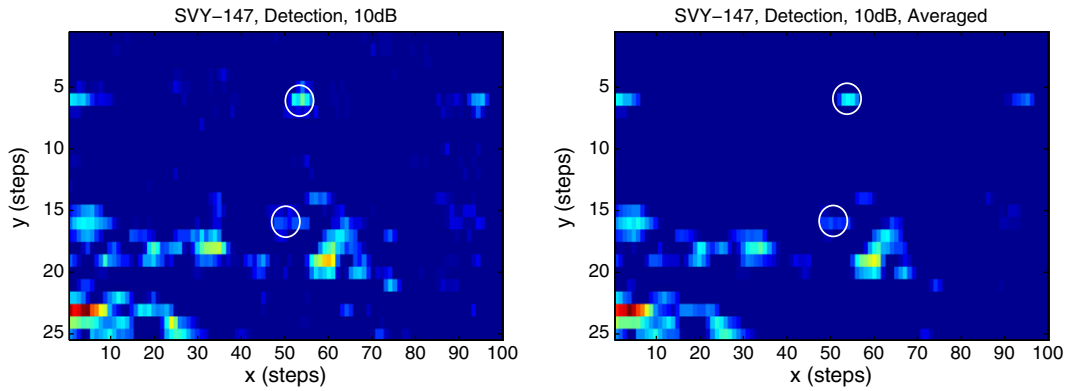
Fig. 9. Detection map without (left) and with IWD averaging (right) over a survey area with buried ERA test targets.

The figures presented show that applying such a technique helps to increase the contrast of the computed detection map as well as to get rid of isolated detections. All this leads to a prominent reduction of the image clutter and substantial increase of the detection rate apart from a remarkable improvement of the target visualization.

At this point the authors would like to remark, that weighted averaging is not applied directly on the resulting detection map but on every slice before the calculation of the final sum over the selected time interval. This is done in this manner because the illuminated pixels in a 2D detection map may come from different depth slices even if they appear very close or overlap. Thus, in order to avoid that direct IDW averaging of this map produces wrong results, it should be previously performed for each of the different depth contributions separately.

Figs. 7, 8, 9 and 10 depict the detection maps of four representative surveys where a pair of PMN simulants, ERA test targets and small Type-72 simulants are buried. The resulting images before and after IDW averaging are illustrated on the left and right side of each figure respectively. Fig. 10 demonstrates that the detection of the smallest targets based only on the amount of scattered energy remains a difficult task, even after the averaging. Nevertheless, the improvement of the images applying this technique became evident in all the surveyed areas.

4.3. Detection-after-Recognition

Sometimes the energy-based detection algorithm does not work well since the backscattered energy by the landmine-like target is of the same order or below the clutter level. This will happen especially for very weak scatterers or for inhomogeneous soils where the clutter average value is high. The incorporation of a preceding processing or filtering step, may help to improve this limitation, removing part of the clutter and hence, increasing the SCR. More specifically, a combined

Detection-after-Recognition algorithm is proposed, whose performance with field data will be analyzed in more detail below.

By means of an initial cross-correlation based filtering, the combined algorithm filters out those A-scans which are not similar enough (above a certain correspondence threshold) to some synthetic reference waveforms, and afterwards, it takes the resulting data volume and searches for the pixels or clusters containing sufficient energy to be relevant. Hence, the detection algorithm is only applied to the A-scans related to target identifications in the class map. The similarity filter considered is defined as follows:

$$|I(x,y;T)| = \begin{cases} |I(x,y;T)| & \text{if } \rho^k(x,y) > \text{Threshold.} \\ 0, & \text{otherwise} \end{cases} \quad (17)$$

where $|I(x,y;T)|$ represents again the absolute value of the time windowed recorded signal and $\rho^k(x,y)$ is the corresponding correlation coefficient with the reference waveform associated to the object k. In this way, much of the clutter contributions are removed and the estimated clutter level is accordingly lowered, resulting in a more efficient landmine detection performance.

The Detection-after-Recognition algorithm has been investigated for the cases with and without IDW averaging in both, the identification and detection steps. Figs. 11, 12, 13 and 14 compare the obtained detection maps for the same surveys analyzed previously. The time window for each of these surveys is the same as when the detection alone was conducted. After a first comparison of the new detection maps with the corresponding ones without the described filtering, an important clutter reduction is observed in all cases.

In general, the SCR is notably higher with the combined algorithm and the detection performance is not penalized. Moreover, for difficult detection cases (weak scatterers), like the surveys SVY-147 and SVY-157, where the test mines were hardly visible applying the detection
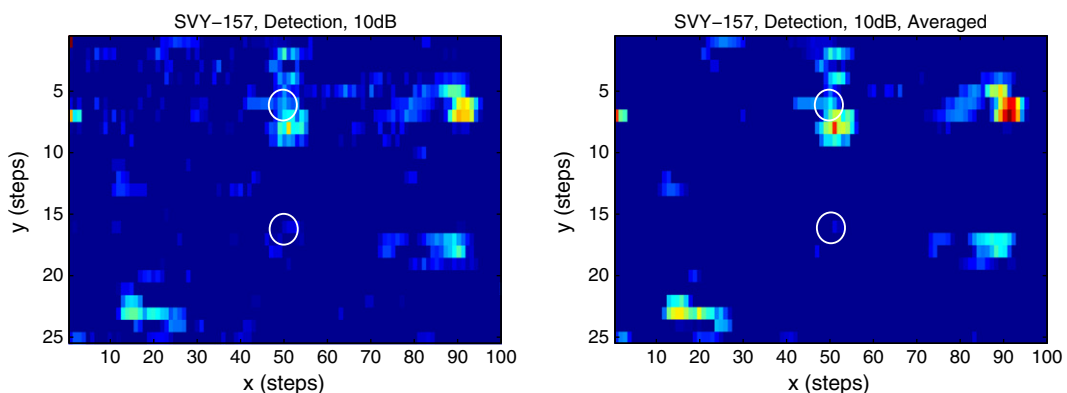

Fig. 10. Detection map without (left) and with IWD averaging (right) over a survey area with buried Type-72 simulants.
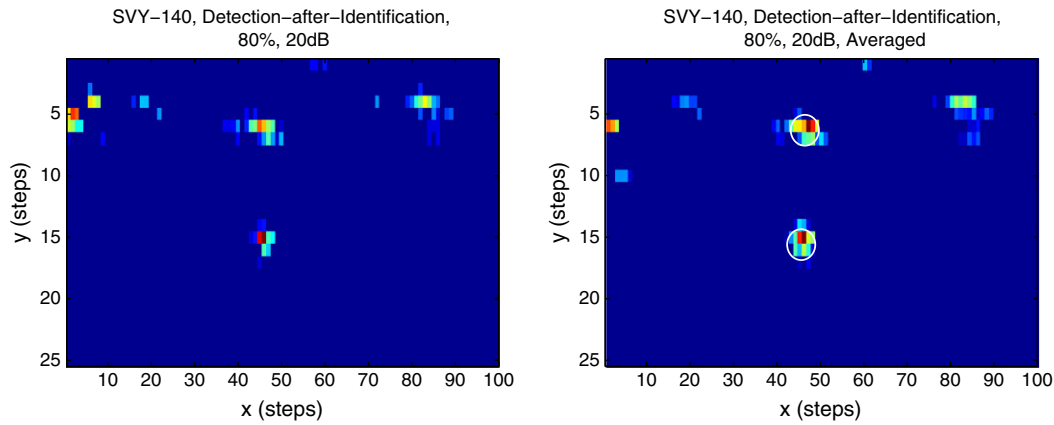
Fig. 11. Detection map after identification without (left) and with IWD averaging (right) over a survey area with buried PMN simulants.

algorithm alone, the performance of the combined algorithm is particularly satisfactory: the mines are now visible, i.e., the detection rate is notably enhanced. It is particularly interesting to observe the SVY-157, where only after detection, none of the Type-72 simulants were visible (see Fig. 10) and a strong reflector was detected very close to the position of the top mine. The energy scattered by this reflector masks totally the echo of the real target and in such a situation it is very difficult to detect the small Type-72 based on the scattered energy amount. However, when looking at the result from the combined algorithm, both mines are clearly visible since the strong reflector contribution (and some others) is already suppressed in the identification step.

On the other hand, from the analysis of both versions of the combined strategy, without (left) and with (right) IDW averaging, a notorious improvement is appreciable in most cases: in general, isolated detections and clutter are efficiently removed, and the contrast of the detections is in general higher, that yields a better visual recognition of the scatterers.

Finally, to assess the potential of the combined strategy to discriminate between targets, Fig. 15 displays the ROC curves obtained after applying the single and the combined algorithm to the surveys with buried PMN, ERA test targets and Type-72 simulants respectively. Each of the plots exhibits the computed ROC curves associated to a group of surveys. The discrimination threshold is the maximum value of the cross-correlation coefficient.

The plot at the top depicts the ROC curves for the biggest of the targets, the PMN simulant. In this case, since the mine contrast is high,

the detection algorithm gives a very low FAR (< 1%) for a Pd of 100%. In that situation, the application of the correlation filter does not improve the curve in any case. This result makes sense since such a filter enhances certain samples, removing some others that don't fulfill the similarity criterion. But the resemblance is measured with respect to a simulated reference wavelet in ideal conditions (homogeneous soil) for a CAD model of the target (which is not an exact copy) and for a given depth. As already seen in the previous section, it has never reached a correlation between the simulation and measurement above 98%. Then, the sensitivity of the similarity measure is below the true positive rate already achieved. However, applying the correlation filter, it is still possible to classify the targets: the true positive rate is the highest for the PMN mine while for Type-72 the ROC curve exhibits the worst values, since the latter is the most dissimilar simulant.

A second example is illustrated in the central plot. Now, the true positive rate applying only the detection algorithm is still satisfactory but worse than in the case of the PMN mine, which is a logic result since the mine is smaller. In this case, after the application of the correlation filter, the true positive rate is improved when the comparison is made with an ERA test target, which is the actual mine. For the other two simulants the curve worsens slightly. In this case the classification of the mines is again successful.

The third example in Fig. 15 (bottom) corresponds to the smallest and most difficult to detect simulant, the Type-72. As it can be seen, in this particular case the detection performance is very unsatisfactory. Simply performing energy-based processing, all the mines cannot be
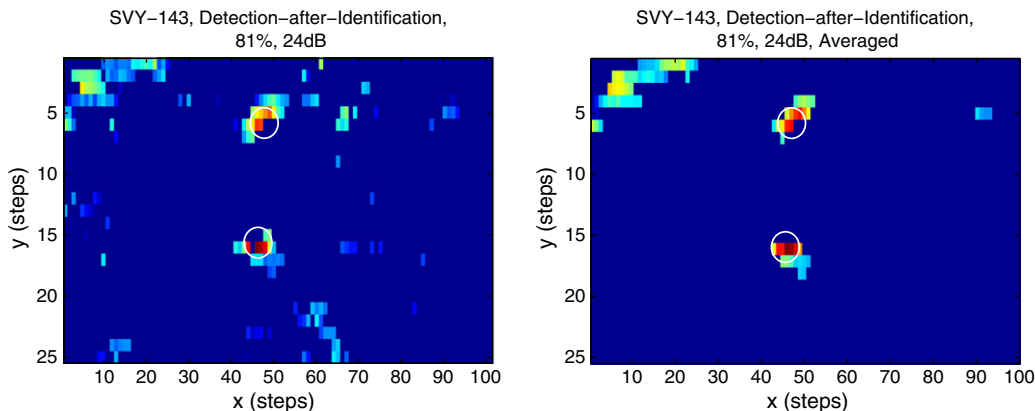

Fig. 12. Detection map after identification without (left) and with IWD averaging (right) over a survey area with buried ERA simulants.
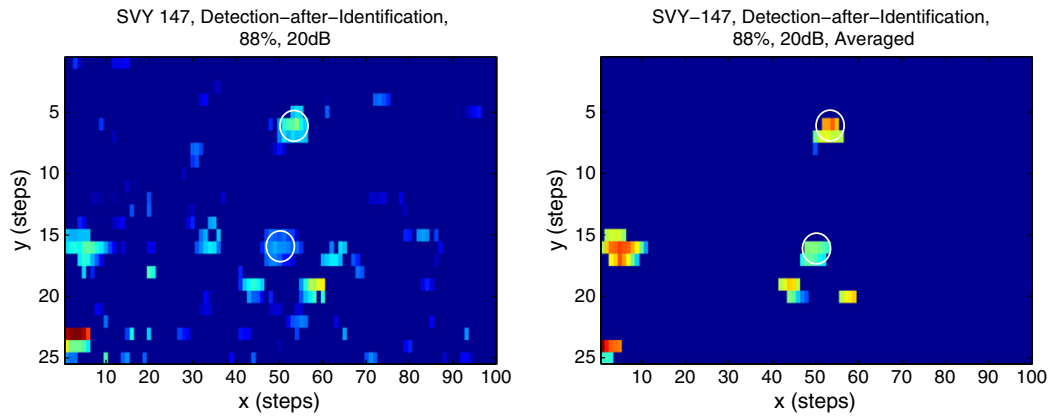
Fig. 13. Detection map after identification without (left) and with IWD averaging (right) over a survey area with buried ERA simulants.

detected even for a low threshold (which gives rise to a high FAR). On the other hand, when the correlation filter is applied, the ROC curves are remarkably improved even for a correlation with a false mine. This is because the mines are relatively similar (in size, shape and composition) objects whose signatures don't differ too much between each other. Consequently, for such a bad performance of the energy detection, filtering the data using the reference signature of any small plastic cylindrical object will most probably bring a better result. In particular, when applying correlation with the Type-72 synthetic waveform, the obtained ROC curve is the best one, achieving for this case 100% detection rate.

We must note, that the reference waveforms considered to carry out the correlation measure were only a first approximation and most probably not enough to be representative. They were computed for a few targets buried either 5 cm or 10 cm deep and antenna height of 6 cm. The soil assumed for the simulation was homogeneous (either dry: $_r = 5$, $\sigma = 0.001$ S/m or wet: $_r = 7$, $\sigma = 0.01$ S/m) while in the test field the soil permittivity values measured with the TDR sensor changed between 4.5 and 11. Moreover, the soil roughness made it impossible to maintain a constant antenna height. Therefore, the obtained results could probably have been better if a more accurate and large collection of simulated signatures had been considered.

Nevertheless, the goal here was not to build a big database, but to demonstrate the potential of adding a similarity filter based on accurate simulations, to reduce the false alarm rate and classify the targets.

Summarizing the presented strategy works fairly well as classifier even for an inhomogeneous scenario and shallow dielectric landmines,

while a substantial false alarm reduction with respect to applying solely energy considerations is accomplished when the ROC curve for the energy detection alone lies above 2% FAR for 100% Pd, i.e., for those landmines that are most difficult to detect (small and low-contrast). These are the situations where more complicated GPR postprocessing algorithms become imperative and this method seems to bring at least part of the solution to problem.

5. Conclusion

The potential application of GPR synthetic target responses for buried landmine identification and clutter suppression has been investigated. The results evidence that adding an initial target recognition step to the energy based detection scheme, may help to enhance the landmine detection rate and reduce the false alarm. In particular, it is demonstrated that the resulting detection maps are better after processing the data volume by a cross-correlation based similarity filter than when considering directly the raw data matrix, since the usually weak scattering responses of the mines are often masked by other unwanted reflections. It is also shown that the integration of a straightforward Inversed Distance Weighted averaging technique into the proposed combined procedure can efficiently improve the visual recognition of buried targets and reduce the clutter contributions. The robustness of the approach under inhomogeneous soil conditions and its capability for discriminating different classes of targets have been also evidenced.
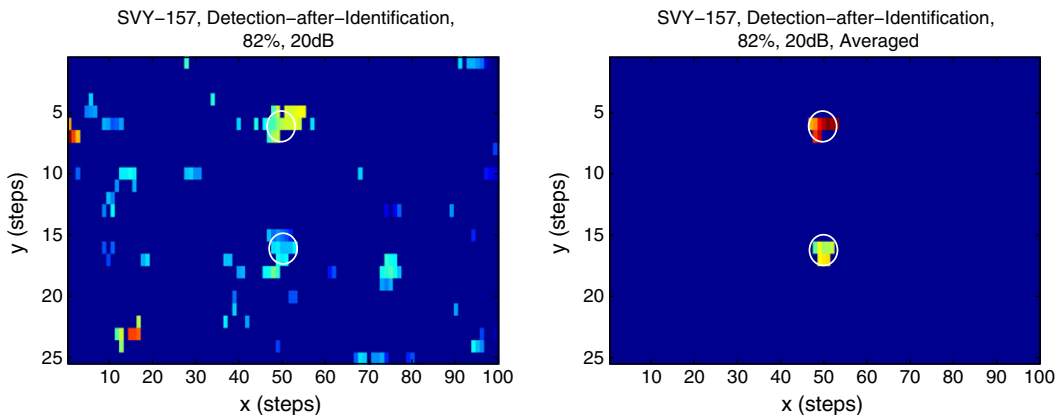

Fig. 14. Detection map after identification without (left) and with IWD averaging (right) over a survey area with buried Type-72 simulants.
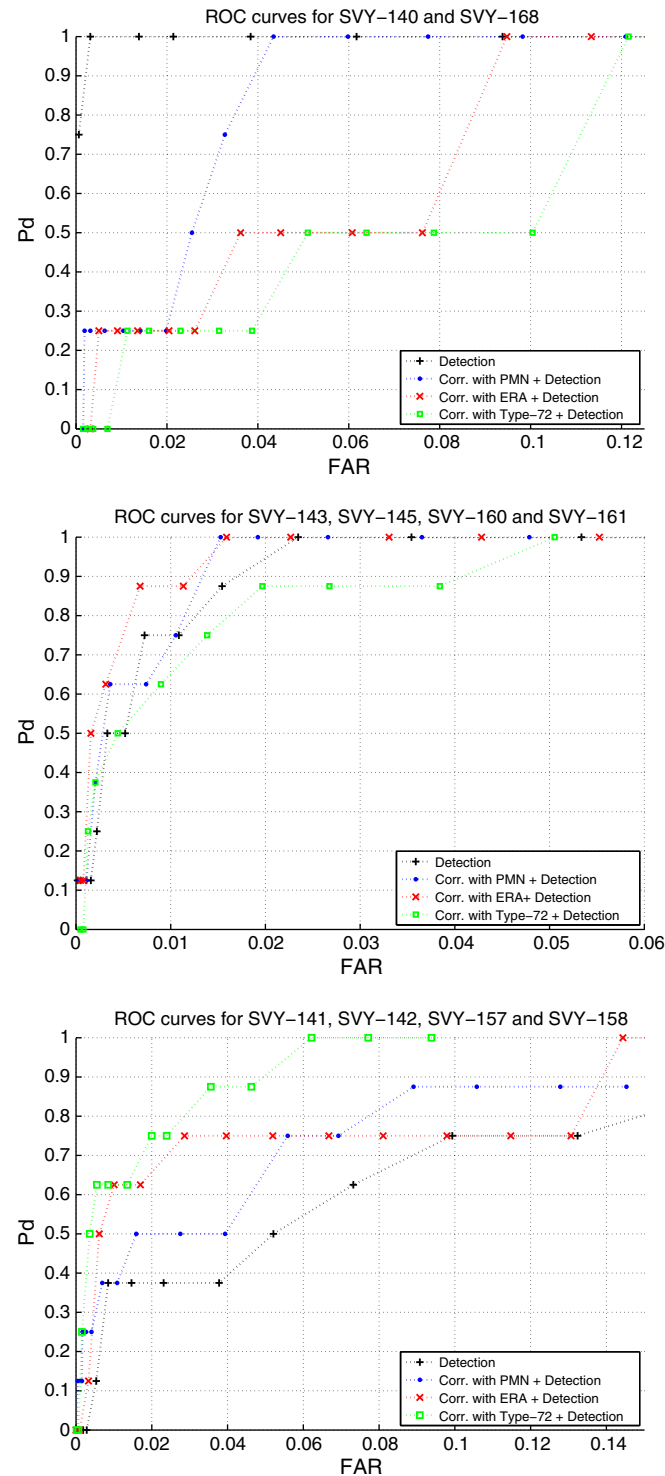
Fig. 15. ROC curves after applying the detection algorithm to the surveys with buried PMN (top), ERA test targets (middle) and Type-72 simulants (bottom).

References

Carevic, D., 2000. Clutter reduction and detection of minelike objects in ground penetrating radar data using wavelets. Subsurf. Sens. Technol. Appl. 1 (1).

Daniels, D.J., 2007. Ground penetrating radar, IEE Radar, Sonar, Navigations and Avionics Series 15, 2nd Edition. The Institution of Engineering and Technology.

Gader, P.D., Mystkowski, M., Zhao, Y., 2001. Landmine detection with ground penetrating radar using hidden Markov models. IEEE Trans. Geosci. Remote Sens. 39 (6).

Gader, P.D., Lee, W.H., Wilson, J.N., 2004. Detecting landmines with ground-penetrating radar using feature-based rules, order statistics, and adaptive whitening. IEEE Trans. Geosci. Remote Sens. 42 (11).

Gonzalez-Huici, Maria A., Uschkerat, U., 2010. GPR modeling for landmine detection. Proc. of the 20th International Symposium on Electromagnetic Theory URSI/ EMTS, Berlin.

Karlsen, B., Sorensen, H.B., Larsen, J., Jakobsen, K.B., 2002. Independent component analysis for clutter reduction in ground penetrating radar data. Proc. SPIE 4742, 378.

Lu, G.Y., Wong, D.W., 2008. An adaptive inverse-distance weighting spatial interpolation technique. Comput. Geosci. 34.

Massa, A., Boni, A., Donelli, M., 2005. A classification approach based on SVM for electromagnetic subsurface sensing. IEEE Trans. Geosci. Remote Sens. 43 (9).

Potin, D., Vanheeghe, P., Duflos, E., Davy, M., 2006. Detection of buried landmines by using an abrupt change detection algorithm. IEEE Trans. Geosci. Remote Sens. 44 (2).

Shao, W., Bouzerdoum, A., 2011. Automatic classification of ground-penetrating-radar signals for railway-ballast assessment. IEEE Trans. Geosci. Remote Sens. 40 (10).

Shao, W., Bouzerdoum, A., Phung, S.L., 2013. Sparse representation of GPR traces with application to signal classification. IEEE Trans. Geosci. Remote Sens. 51 (7).

Shepard, D., 1968. A two-dimensional interpolation function for irregularly-spaced data. Proc. of the 1968 23rd ACM National Conference.

Uschkerat, U., 2000. Mine detection using a maximum likelihood estimator and in-field GPR data. Proc. of the IEEE International Radar Conference.

von Hippel, A., 2005. Dielectric materials and applications. Artech House, 1995, Electromagnetic Module, User's Guide.

Wilson, J.N., Gader, P., Lee, W.H., Frigui, H., Ho, K.C., 2007. A large-scale systematic evaluation of algorithms using ground-penetrating radar for landmine detection and discrimination. IEEE Trans. Geosci. Remote Sens. 45 (8).

Yang, C.C., Bose, N.K., 2005. Landmine detection and classification with complex-valued hybrid neural network using scattering parameters dataset. IEEE Trans. Neural Networks 16 (3).